J A C S
JOURNAL OF THE AMERICAN CHEMICAL SOCIETY
ARTICLE
pubs.acs.org/JACS

Porous Organic Cage Nanocrystals by Solution Mixing

Tom Hasell, Samantha Y. Chong, Kim E. Jelfs, Dave J. Adams, and Andrew I. Cooper*

Department of Chemistry and Centre for Materials Discovery, University of Liverpool, Crown Street, Liverpool L69 7ZD, U.K.

S *Supporting Information* W *Web-Enhanced*

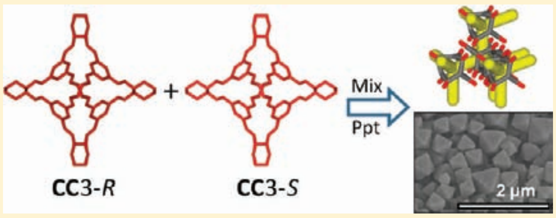

ABSTRACT: We present here a simple method for the bottom-up fabrication of microporous organic particles with surface areas in the range 500−1000 m^2 g^{-1}. The method involves chiral recognition between prefabricated, intrinsically porous organic cage molecules that precipitate spontaneously upon mixing in solution. Fine control over particle size from 50 nm to 1 μm can be achieved by varying the mixing temperature or the rate of mixing. No surfactants or templates are required, and the resulting organic dispersions are stable for months. In this method, the covalent synthesis of the cage modules can be separated from their solution processing into particles because the modules can be dissolved in common solvents. This allows a "mix and match" approach to porous organic particles. The marked solubility change that occurs upon mixing cages with opposite chirality is rationalized by density functional theory calculations that suggest favorable intermolecular interactions for heterochiral cage pairings. The important contribution of molecular disorder to porosity and surface area is highlighted. In one case, a purposefully amorphized sample has more than twice the surface area of its crystalline analogue.

INTRODUCTION

Microporous materials with pores smaller than 2 nm have potential applications in sorption, in separation, and in heterogeneous catalysis.[1,2] Most microporous solids are extended networks, such as metal−organic frameworks (MOFs),[3−7] covalent organic frameworks (COFs),[8−14] or organic polymer networks.[15−19] Much attention has focused on control over pore size, surface area,[20] and functionality in microporous solids. However, the physical form and morphology of the material can be equally important in many applications. Porous membranes might be desirable for gas separations,[21,22] while porous particles may be more suitable in heterogeneous catalysis,[23] chromatographic separations,[24] and drug delivery[25] or for the preparation of hierarchically porous solids.[26]

For porous particles, size and shape control is important—for example, to modulate mass transport of guests in and out of the solid, or to produce materials which can be packed effectively as chromatographic stationary phases. Likewise, control over particle dispersibility in liquids may be required in applications such as drug delivery.[25] Two main approaches exist for particle size control in porous solids: top-down processing, and bottom-up synthesis. The most common top-down processing methods are grinding, milling, and sieving, and these can also be applied to porous materials.[27−29] Bottom-up synthesis methods include direct crystallization from reaction solutions,[30−32] ultrasonic or microwave synthesis,[33] solvent-free synthesis,[34] seeded nucleation,[35] crystallization within prefabricated polymer monoliths[36] or beads,[37] and heterogeneous polymerization.[38] In the context of crystalline porous solids, zeolites have been investigated most widely in terms of particle size control,[39] and methods include templated synthesis,[40−43] hydrothermal crystallization,[44,45] and confined-space synthesis.[46,47] More recent studies have described particle size control for other microporous frameworks such as MOFs,[48] porous coordination polymers,[49] and infinite coordination polymers.[50]

For nanoscale porous particles, the contribution of the external particle surface is no longer negligible. This can be expected to influence sorption behavior, although this is not always considered.[13,49] For crystalline porous solids such as MOFs and COFs, sorption properties are often related directly to crystal structure data with no consideration of the influence of particulate morphology. This is a reasonable approximation for larger crystals with high micropore surface areas, but becomes increasingly less valid as particle sizes are reduced. Particle size control for porous solids can be used to influence the interplay between sorption into micropores and interparticle voids, thus leading to hierarchical materials comprising both microporosity and mesoporosity.[39,40] Also, diffusion lengths for mass transport are decreased in nanosized porous materials, and this is important, for example, in catalysis[49] and in separations. Substantial effort has been made recently to produce small-scale porous MOF crystals, but this is still seen as challenging. Newly developed methods, whether using surfactants,[51] confined space synthesis,[52,53] or tuning of reaction conditions,[54,55] still struggle to achieve monodisperse crystal sizes, and to obtain truly nanoscale crystals with diameters of 100 nm or less. Moreover, such methods often require complex workup and purification procedures to remove the surfactant or template.

In addition to the various classes of porous networks mentioned above, there is growing interest in porous materials composed of discrete organic[56−68] or metal−organic[69,70] molecules. For example,

Received: September 28, 2011
Published: November 14, 2011

dx.doi.org/10.1021/ja209156v | *J. Am. Chem. Soc.* 2012, 134, 588–598

Scheme 1. Synthesis of Organic Cage Modules by [4+6] Cycloimination Reactions[a]

[a] Both cage modules **CC3** and **CC4** can be produced as either *R* or *S* enantiomers by using the (*R*,*R*)- or (*S*,*S*)-diamines, respectively. For clarity, only the (*R*,*R*)-diamines and cage products are shown.

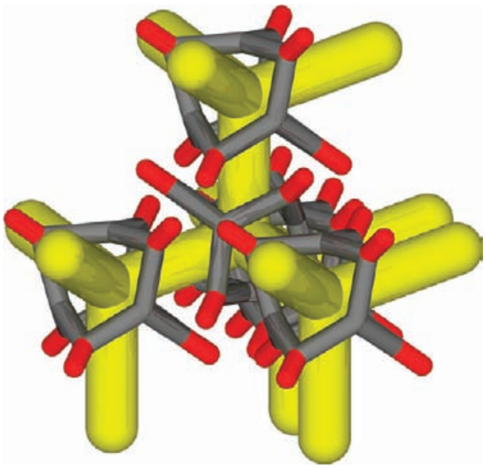

Figure 1. Scheme showing the window-to-window cage−cage packing that leads to a 3-D diamondoid interconnected pore network (in yellow) in the crystal structure for **CC3**-*R*.

we reported a class of [4+6] cycloimine cage compounds (Scheme 1) which show gas uptakes that are remarkable for molecular organic crystals.[59,66]

The cages have tetrahedral symmetry and include four windows that are large enough to be penetrated by small molecules such as gases,[59,66] halogens,[68] and organic solvents.[65] This inherent porosity leads to high levels of permanent microporosity in the molecular crystals after desolvation, with apparent Brunauer−Emmett−Teller surface areas (SA_{BET}) up to 624 m^2 g^{-1} for our first generation of cages (produced from 1,3,5-triformylbenzene; see Scheme 1),[59] and exceeding 1300 m^2 g^{-1} for expanded analogues prepared by our group[66] and by Mastalerz et al.[62] Variation of the vertex functionality in the cages controls both the crystal packing and the topology of the resulting pore network. For example, the homochiral (*R*,*R*)-1,2-diaminocyclohexane cage, **CC3**-*R*, packs in a window-to-window arrangement to generate a 3-D diamondoid pore network (Figure 1).[59] By contrast, the (*R*,*R*)-1,2-diaminocyclopentane derivative, **CC4**-*R*, packs via window-to-arene interactions,[71] despite its close structural similarity with **CC3**-*R*. This leads to frustrated crystal packing and a more complex pore structure in **CC4**-*R*. [To summarize the notation, **CC*n***-*Y* refers to covalent cage ***n*** with chirality *Y*. The racemate of **CC*n*** is therefore **CC*n***-(*R*,*S*), and quasi-racemates are (**CC*n***-*R*, **CC*m***-*S*).]

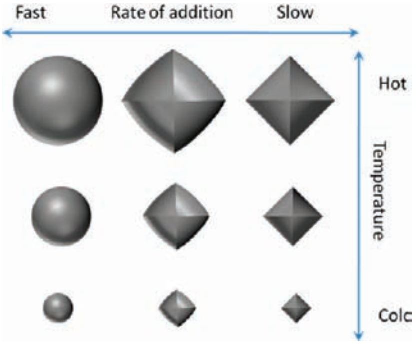

Figure 2. Scheme illustrating size and morphology control in porous organic crystals, as achieved by varying the mixing rate and the mixing temperature.

A distinguishing feature of "porous organic molecules"[61] is that they can be dissolved in common solvents. This opens up a range of processing options that are not available for insoluble networks and frameworks. We exploit this here to produce porous crystals with exceptional control over particle size and morphology. The method involves mixing prefabricated porous cage modules that precipitate rapidly from solution as a result of chiral recognition.[66] Fine control over particle size is achieved in a size range from 50 nm to a few micrometers, without the addition of any surfactants or additional templates. Both the mixing temperature and the rate of mixing may be used to control the crystallization process and, thus, the size and shape of the porous particles (Figure 2). The method can be applied both to racemic crystals, comprising a single cage module, and to quasi-racemic[72] cocrystals comprising more than one module, in both cases using intermolecular chiral recognition to drive the particle precipitation. These porous particles can have apparent BET surface areas (up to ~950 m^2 g^{-1}) that exceed those observed for solids produced from the individual component cage modules. We also examine the percentage crystallinity in these particles, and show that molecular disorder can increase rather than decrease the accessible pore volume. This latter effect, which may not be immediately obvious from measurements such as powder X-ray diffraction (PXRD), might have broader implications with respect to other microporous materials, such as COFs.[8−14]

■ METHODS

Cage Synthesis. For **CC3**-*R*, dichloromethane (DCM, 100 mL) was added slowly onto solid 1,3,5-triformylbenzene (5.0 g, 30.86 mmol) without stirring at room temperature. Trifluoroacetic acid (100 μL) was added directly to this solution as a catalyst for imine bond formation. Finally, a solution of (*R*,*R*)-1,2-diaminocyclohexane (5.0 g, 44.64 mmol) in DCM (100 mL) was added. The unmixed reaction was covered and left to stand. Over 5 days, all of the solid triformylbenzene was consumed, and octahedral crystals grew on the sides of the vessel. The crystalline product was removed by filtration and washed with 95% ethanol/5% DCM. Yield: 6.5 g, 83%. The synthesis of **CC3**-*S* was identical to that of **CC3**-*R*, apart from the use of the (*S*,*S*)-1,2-diaminocyclohexane diastereomer. ^{1}H NMR ($CDCl_3$): δ 8.15 (s, C*H*=N, 12H), 7.89 (s, ArH, 12H), 3.33 (m, C*H*N, 12H), 1.9−1.4 (m, CH_2, 48H) ppm. ^{13}C NMR ($CDCl_3$): δ 159.1, 136.7, 129.5, 74.7, 33.0, 24.4 ppm. MS (ES+): 1118 ([M+H]$^+$). Accurate mass calculated for $C_{72}H_{85}N_{12}$: 1117.7020. Found: 1117.7065.

For **CC4**-*S*, (*S*,*S*)-1,2-cyclopentadiamine dihydrochloride (1.038 g, 6.0 mmol) and triethylamine (0.85 mL, 6.0 mmol) were dissolved in methanol (80 mL). The resulting solution was added dropwise over a stirred solution of 1,3,5-triformylbenzene (648 mg, 4.0 mmol) in DCM (80 mL). The resulting mixture was left covered for 10 days at 20 °C. White, needle-like crystals of **CC4**-*S* were collected by filtration, washed with DCM/methanol (5:95 v/v) mixture, and dried in air. Yield: 898 mg, 87%. ^{1}H NMR ($CDCl_3$): δ 8.20 (s, C*H*=N, 12H), 7.92 (s, ArH, 12H), 3.73 (m, C*H*N, 12H), 1.98 (m, CH_2, 36H) ppm. ^{13}C NMR ($CDCl_3$): δ 160.1, 136.5, 129.6, 78.3, 31.8, 21.1 ppm. MS (ES+): 1033.6 ([M+H]$^+$).

Mixing of Cage Solutions. Solutions of the various cage modules were mixed using an automated liquid handling robot (Chemspeed Technologies ASW2000) in order to achieve reproducible control over the addition parameters. A solution of **CC3**-*S* in DCM (1.34 mM, 1.5 mg/mL) was added to a solution of either **CC3**-*R* in DCM (1.34 mM, 1.5 mg/mL) or **CC4**-*R* in DCM (1.34 mM, 1.387 mg/mL) at a rate of 0.5 mL min^{-1} with continuous vortex mixing at a speed of 400 rpm. The mixing temperature was altered by heating/cooling the reaction vessels on the liquid handling stage. A total volume of 6 mL was used for the majority of the samples, but this was increased to 50 mL to produce enough material for gas sorption analysis. For the investigation of solvent addition rates, the temperature was maintained at 20 °C and the rate of addition adjusted to 0.5, 5, or 20 mL min^{-1}.

Characterization. *NMR.* Solution ^{1}H NMR spectra were recorded in deuterated chloroform at 400.13 MHz using a Bruker Avance 400 NMR spectrometer.

Electron Microscopy. Imaging of the crystal morphology was achieved using a Hitachi S-4800 cold field emission scanning electron microscope (FE-SEM) operating in both scanning and transmission modes. Scanning-mode samples were prepared by depositing dry crystals on 15 mm Hitachi M4 aluminum stubs using an adhesive high-purity carbon tab before coating with a 2 nm layer of gold using an Emitech K550X automated sputter coater. Imaging was conducted at a working distance of 8 mm and a working voltage of 3 kV using a mix of upper and lower secondary electron detectors. Transmission-mode samples were prepared by dispersing the cage particles in a methanol suspension and depositing onto carbon-coated copper grids (300 mesh), imaging at 30 kV working voltage and 7 mm distance.

Powder X-ray Diffraction. PXRD data were collected in transmission mode on a Bruker Advance D8 diffractometer with Ge-monochromated Cu Kα_1 radiation and a LynxEye PSD on samples held in 1 mm diameter special glass capillaries. High-resolution synchrotron PXRD data were collected on the I11 beamline at Diamond Light Source (λ = 0.826141 Å) in transmission geometry using a capillary spinner. Analysis of the powder diffraction patterns was carried out using TOPAS-Academic[73] software.

Details of density functional theory (DFT) calculations and crystal morphology predictions are provided in the Supporting Information.

Gas Sorption Analysis. Surface areas were measured by nitrogen adsorption and desorption at 77.3 K. Powder samples were degassed offline at 100 °C for 15 h under dynamic vacuum (10^{-5} bar) before analysis, followed by degassing on the analysis port under vacuum, also at 100 °C. Isotherms were measured using a Micromeritics 2020 or 2420 volumetric adsorption analyzer.

Dynamic Light Scattering. Analysis was performed directly on the mixed cage solutions in DCM using quartz vials and a Malvern Instruments Zetasizer nano series.

RESULTS

Particle Formation by Mixing Solutions of Cage Modules. Two separate, equimolar solutions of **CC3**-*R* and **CC3**-*S* (1.34 mmol) were prepared in either DCM or chloroform. When these solutions were mixed at room temperature, it was observed that the combined solution became cloudy within seconds (Figure 3a; see the video of the mixing process online). This is surprising, since the total cage concentration is unchanged upon mixing. The precipitation is caused by a sharp decrease in solubility upon mixing of the *R* and *S* enantiomers. This was confirmed by ^{1}H NMR studies which showed the racemic mixture to be at least 10 times less soluble than the separate chiral modules (see Supporting Information, Figure S1; saturation solubility of **CC3**-*R* in $CHCl_3$ = 8 mmol/L ; equivalent solubility of **CC3**-(*R*,*S*) racemate = 0.7 mmol/L). A Job plot produced from NMR data at various **CC3**-*R*/**CC3**-*S* ratios also confirmed that the solubility was lowest at a 1:1 molar ratio of the two enantiomers (Figure S2). This phase behavior is a physical manifestation of the strong preference for heterochiral window-to-window packing between the two modules, as rationalized previously by crystal structure prediction (CSP) methods.[66,74,75]

Particle Size Control Using Mixing Temperature. The degree of opacity was reduced for a given starting concentration when the solutions of **CC3**-*R* and **CC3**-*S* were mixed at lower temperatures (Figure 3a, right). Moreover, solutions mixed at reduced temperatures showed a slight blue coloration, indicative of the light scattering that occurs with nanoscale particles. The effect of temperature on particle size was therefore investigated in detail by combining **CC3**-*R* and **CC3**-*S* at various mixing temperatures. All other conditions, such as concentration and rate of mixing, were kept constant. The resultant particle size was measured by dynamic laser scattering (DLS) and also by scanning electron microscopy (SEM) (Figure 3b,c). The **CC3**-(*R*,*S*) particles were relatively monodisperse in size at all mixing temperatures between −80 and +5 °C, and ranged from less than 100 nm, at low temperature, to more than 1 μm at close-to-ambient temperatures. That is, the size of the particles can be controlled systematically by varying the mixing temperature. As discussed below, all samples were highly microporous. There was excellent agreement between the SEM and DLS results (Figure 3b), at least up to around 1 μm, above which size the DLS measurement becomes less reliable. All of the particle dispersions were found to be stable in DCM for at least several months, with no Ostwald ripening or changes in particle size (Figure 3d). The decrease in particle size with decreasing mixing temperature stems, presumably, from a combination of decreased solubility, lower diffusivity, and rapid nucleation that results in the growth of more numerous and smaller particles.

The particles are uniform, octahedron-shaped crystals (Figure 4), and this morphology is retained down to the nanoscale (Figure 4b). Each particle appears, superficially, to comprise a discrete, single crystal, rather than aggregated crystals or fragments of larger crystals.

As a control experiment, off-stoichiometry solutions of **CC3**-*R* and **CC3**-*S* were combined in a 3:1 mol:mol ratio, and the precipitated product was filtered off. Both the precipitate and the material in the filtrate were isolated and investigated by PXRD (Figure S3). The material recovered from the filtrate gave only the diffraction pattern of homochiral **CC3**-*R*, while the precipitate gave the peak-shifted diffraction pattern attributed to the racemic **CC3**-(*R*,*S*) crystal, again confirming that the racemate has much lower solubility. The evaporated, as-prepared solution (without the filtration step) gave both sets of diffraction patterns at an approximate 1:1 ratio. This is in agreement with the NMR evidence that the opposite chiral enantiomers combine to form a 1:1 racemic crystal. As such, any remaining, excess homochiral

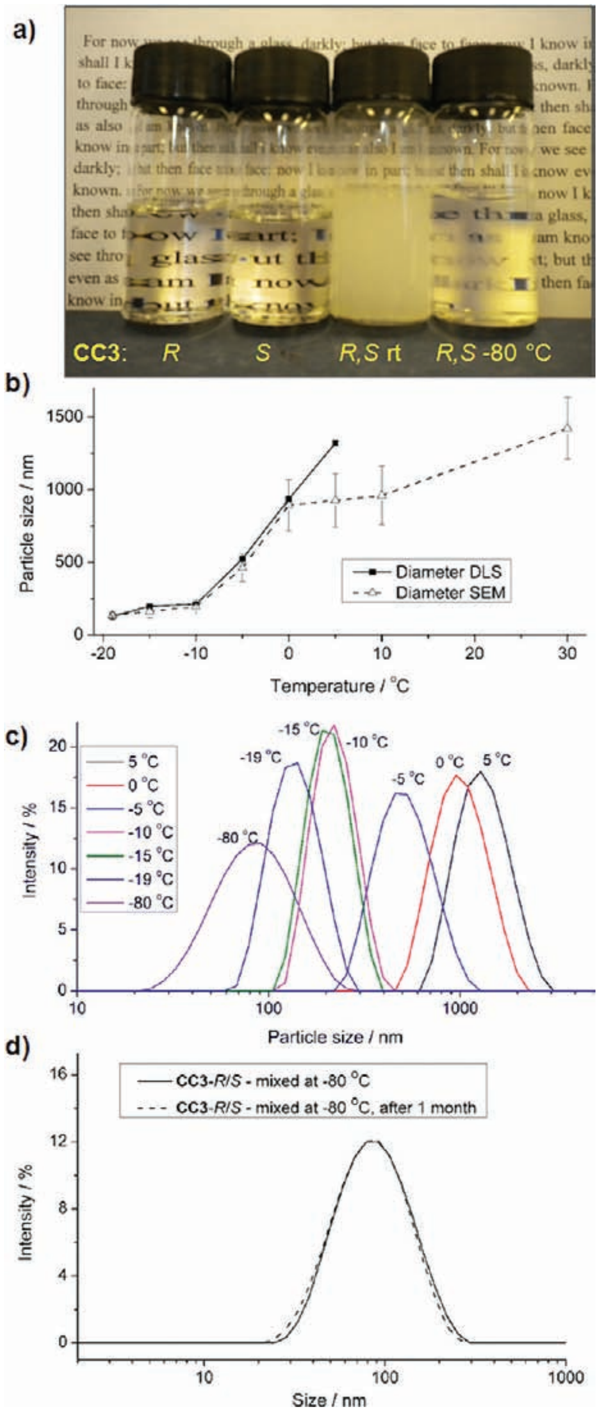

Figure 3. Ⓦ (a) Photograph showing the effect of mixing together equimolar dichloromethane solutions of **CC3**-*R* (far left) and **CC3**-*S* (second from left) at 20 °C to form racemic microcrystals of **CC3**-(*R*,*S*) ($d \approx 1\ \mu$m), causing the solution to become opaque (third vial from left). When the solutions are mixed at −80 °C, a transparent nanodispersion is formed (far right). A video of the 20 °C mixing process is included online. (b) Average particle size as a function of mixing temperature, as measured by DLS and by SEM analysis. (c) Particle size distributions from DLS. (d) DLS measurements show no significant change in particle size after 1 month in DCM solution at room temperature.

cage (**CC3**-*R* in this case) remains in solution, rather than precipitating along with the racemic crystals.

Mixing solutions of the analogous cyclopentane-derivatized modules **CC4**-*R* and **CC4**-*S* (Scheme 1) yields a crystalline, racemic precipitate in the same fashion (Figures S4−S6). Moreover, combining the **CC3**-*R* module with its quasi-racemic cyclopentane analogue, **CC4**-*S*, results in the same behavior (Figure 5). Hence, chiral recognition can be used to produce both porous racemic particles, comprising one module (**CC3** or **CC4**), and quasi-racemic particles, containing two different cage modules (**CC3** and **CC4**). It should be noted that solution NMR spectra for a homochiral mixture of **CC3**-*R* and **CC4**-*R* (or **CC3**-*S* and **CC4**-*S*) show the distinct NMR signals for both species. However, when the heterochiral equivalents of **CC3** and **CC4** are mixed, the NMR spectra for both modules disappear, and no cage signals are detectable (Figure S7). This shows that an even more pronounced drop in solubility occurs when mixing **CC3**-*R* and **CC4**-*S*, and that the change in phase behavior is driven by the chirality, and not the differing chemical functionalities in **CC3** and **CC4**. Again, the particles had octahedral geometries, and particle size could be controlled by varying the mixing temperature, though the effect was less pronounced (Figures 5 and S8), perhaps because of the stronger solubility suppression in the **CC3**-*R*/**CC4**-*S* system.

PXRD patterns for the pure homochiral **CC3** and **CC4** modules, along with the porous racemic particles, **CC3**-(*R*,*S*) and **CC4**-(*R*,*S*), and the quasi-racemic combination, **CC3**-*R* and **CC4**-*S*, are compared in Figure 6a. The PXRD patterns for the racemic and quasi-racemic combinations suggest phase-pure materials. The PXRD patterns for the racemates and quasi-racemate all closely resemble that observed for homochiral **CC3**, suggesting a similar crystal packing, but the peak angles are displaced slightly in each case due to small changes in the unit cell volume. This confirms that the cages combine to form a single racemic or quasi-racemic cocrystal phase, rather than a chiral conglomerate. The shifts observed in the diffraction peaks to higher angles with respect to **CC3** place the unit cell sizes in the following order: **CC3**-*R* > **CC3**-(*R*,*S*) > (**CC3**-*R*, **CC4**-*S*) > **CC4**-(*R*,*S*). This sequence can be rationalized by two simple hypotheses: (i) Opposite enantiomers are able to pack together more tightly in a more energetically favorable arrangement. (ii) **CC4**, being the smaller module, packs more tightly than **CC3**. From PXRD data alone, it is not possible to distinguish unambiguously between an alternating, quasi-racemic structure, as observed previously for the cocrystal (**CC1**-*S*, **CC3**-*R*),[66] and a disordered cubic model where there is 50:50 site occupancy (Figures S5 and S6).

The structure for desolvated **CC4**-(*R*,*S*), as determined from PXRD data, shows that chiral recognition between the two enantiomers directs the system to crystallize in cubic symmetry with the window-to-window packing motif, analogous to **CC3** (Figures 1, S5, and S6).[66] This packing is unlike the window-to-arene "stacks" and trigonal symmetry observed for the homochiral **CC4** system (Figure 6b), as determined by single-crystal X-ray diffraction.[71] These two different packing modes explain the large differences observed in the PXRD patterns for homochiral **CC4**-*S* and **CC4**-(*R*,*S*) (Figure 6a). This can be contrasted with the homochiral **CC3**-*R* and racemic **CC3**-(*R*,*S*) pairing, where cubic window-to-window packing is observed in both cases. Hence, the PXRD data are similar (Figure 6a) to those for homochiral **CC3**, apart from a small shift in the peak positions to higher angles for the racemate, **CC3**-(*R*,*S*).

Rationalization of Particle Formation. Previously, we rationalized the racemic preference for **CC3** using CSP methods,[66]

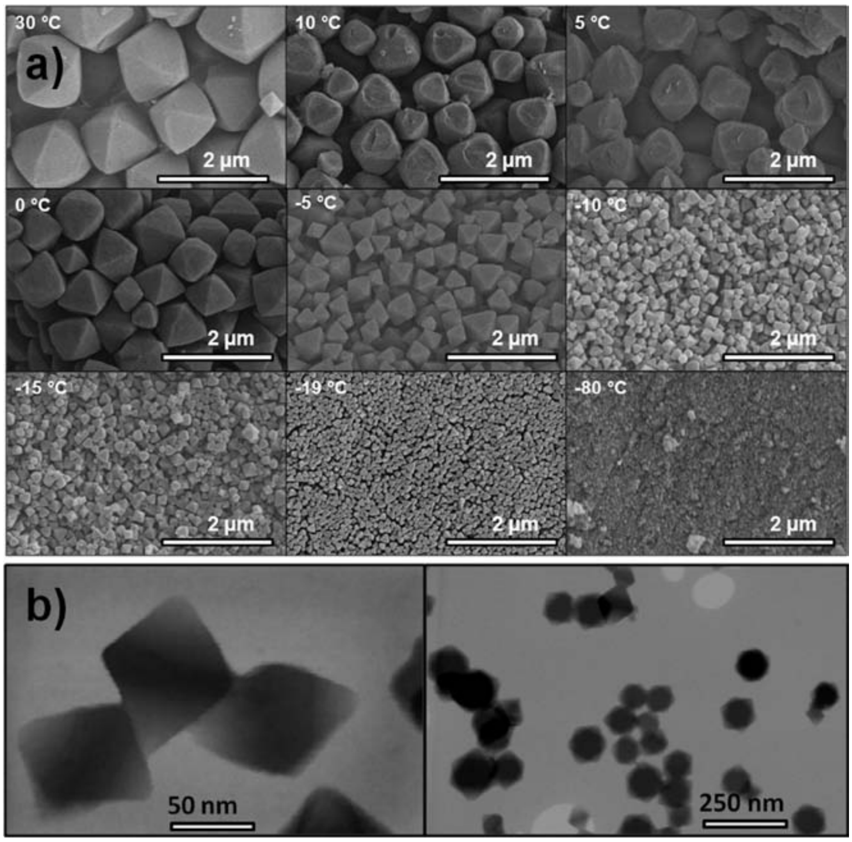

Figure 4. (a) Scanning electron micrographs for racemic **CC3**-(*R*,*S*) crystals formed by mixing dichloromethane solutions of the homochiral **CC3**-*R* and **CC3**-*S* modules at a range of different temperatures. The crystals have octahedral geometry and decrease in size as a function of decreasing mixing temperature. All micrographs are shown at the same scale. (b) Transmission electron micrographs for racemic **CC3**-(*R*,*S*) nanocrystals formed at −20 °C. The crystals have an average diameter of 130 nm.

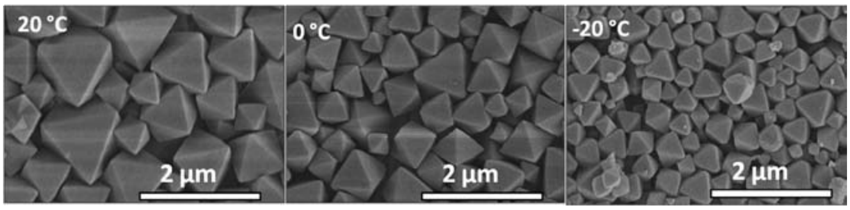

Figure 5. Scanning electron micrographs of quasi-racemic (**CC3**-*R*, **CC4**-*S*) cocrystals formed by mixing dichloromethane solutions of the homochiral **CC3**-*R* and **CC4**-*S* modules at three different temperatures. The cocrystals have octahedral geometry and decrease in size as the mixing temperature is decreased. All micrographs are shown at the same scale.

which calculate the lattice energies for different hypothetical crystal packings. While CSP can give an accurate survey of crystal energy landscapes,[74,75] it is still rather computationally expensive to apply it to multiple molecular combinations, as in this study, especially when the component cage molecules, **CC3** and **CC4**, are relatively large (MW > 1000 g mol^{-1}). We therefore carried out some more restricted DFT calculations for isolated cage pairs to see whether we could explain the preferred packing modes in terms of the most favorable pairwise intermolecular interactions. Table 1 lists the DFT-D3 binding energies for isolated cage pairs calculated in CP2K[76] with the BLYP functional[77] and TZVP-MOLOPT basis sets.[78]

For all three mixed chirality systems—the **CC3** and **CC4** racemates, and the **CC3**/**CC4** quasi-racemate—we calculate significantly more favorable cage-dimer binding energies for the heterochiral packing mode in comparison with homochiral packing. The calculated pairwise energy gains for a racemic or quasi-racemic interaction over a homochiral interaction are 19 (**CC3**), 33 (**CC4**), and 35 kJ mol^{-1} (**CC3**/**CC4**), respectively. While these DFT-D3 dimer calculations do not, of course, express the whole lattice energy, we propose that this strong preference for intermolecular heterochiral pairing is a major contributor to the rapid precipitation that is observed upon mixing of heterochiral modules. This trend in binding energies for heterochiral dimers with respect to homochiral cage dimers rationalizes the marked decrease in solubility that occurs when cages of opposite chirality are mixed (Figures S1 and S2). These DFT calculations also rationalize correctly the observed packing modes for the various module combinations, with all systems preferring window-to-window packing, apart from homochiral

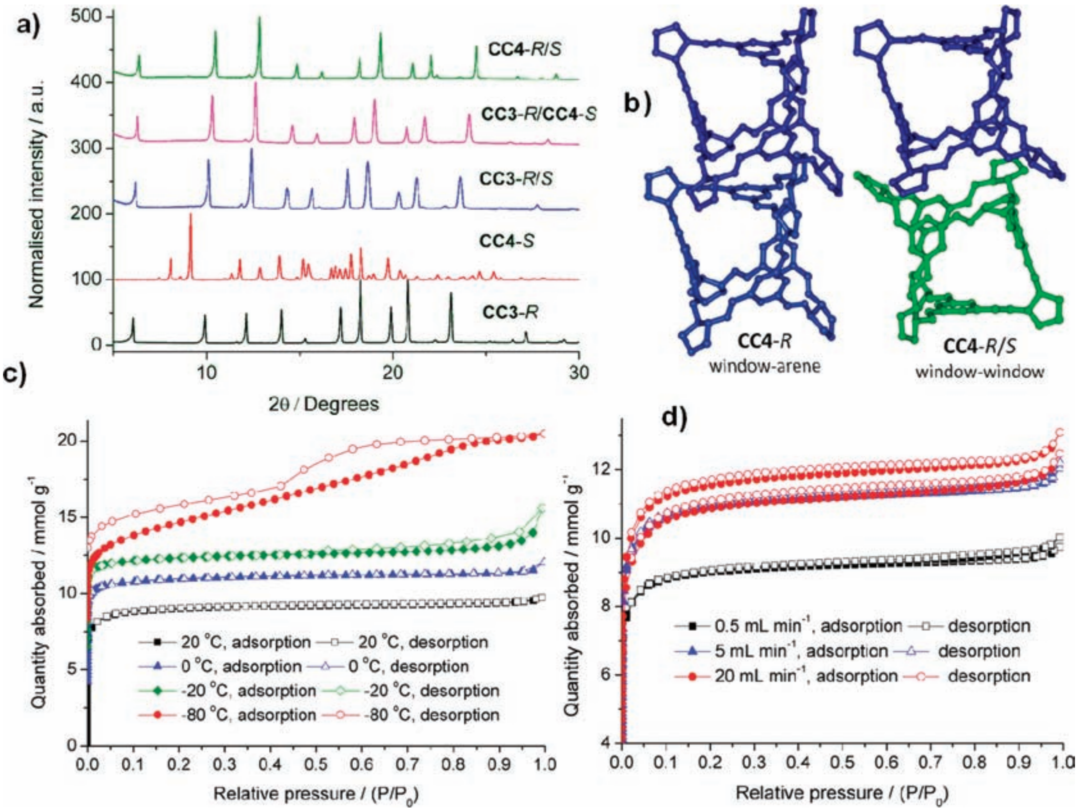

Figure 6. (a) Powder X-ray diffraction patterns for the homochiral forms of **CC3** and **CC4** (patterns for *R* and *S* are identical), compared with racemic and quasi-racemic combinations. (b) Comparison of cage packing modes observed for homochiral **CC4** and racemic **CC4**-(*R*,*S*) crystals. Homochiral **CC4** forms window-to-arene stacks, while racemic **CC4**-(*R*,*S*) adopts a window-to-window packing arrangement, as observed for **CC3**. (c) Nitrogen sorption/desorption isotherms for racemic **CC3**-(*R*,*S*) crystals prepared by mixing at different temperatures, measured at 77 K, offset for clarity by 0, 4, 6, and 8 mmol g^{-1}, for solutions mixed at 20, 0, −20, and −80 °C, respectively. The BET surface areas derived from these adsorption isotherms for the different mixing temperatures are as follow: 20 °C, 696 $m^2\ g^{-1}$; 0 °C, 617 $m^2\ g^{-1}$; −20 °C, 559 $m^2\ g^{-1}$; −80 °C, 507 $m^2\ g^{-1}$. (d) Nitrogen sorption/desorption isotherms for **CC3**-(*R*,*S*) crystals prepared by mixing at 20 °C at different rates of addition, as measured at 77 K (two repeat experiments at each addition rate are shown to demonstrate reproducibility of the preparations). The BET surface areas derived from the adsorption isotherms are as follows: for 0.5 mL min^{-1}, 777 and 776 $m^2\ g^{-1}$; for 5 mL min^{-1}, 948 and 940 $m^2\ g^{-1}$; for 20 mL min^{-1}, 995 and 936 m g^{-1}.

CC4, where window-to-arene packing is energetically preferred by more than 50 kJ mol^{-1} (Figure 6b).[71] We also note that triply interpenetrated cage catenane dimers prefer to interlock in a heterochiral fashion,[79] by close analogy with the "free" cage dimer calculations presented here.

Porosity Analysis. Gas sorption measurements for racemic **CC3**-(*R*,*S*) particles showed that all materials were highly microporous (Figure 6c). Apparent BET surface areas for the samples produced at different mixing temperatures (507−696 $m^2\ g^{-1}$) were broadly comparable with those measured for their homochiral equivalent, **CC3**-*R* (624 $m^2\ g^{-1}$).[59] The shapes of the isotherms, however, were affected by the particle size. An increase in external surface area was observed as the mixing temperature decreased and the particle size was reduced, as evidenced by the upturn in gas uptake at high relative pressure (Figures 6c and S9). The isotherm for the smallest particles, produced at −80 °C ($d_{av} < 100$ nm), deviates from classic type I isotherm behavior,[80] and substantial hysteresis is observed, most likely due to a significant contribution from interparticle voids that occurs as the particle size is reduced to the nanoscale.

CC4-(*R*,*S*) particles, produced by mixing at 20 °C, were also found to give a classic type I isotherm and an apparent SA_{BET} = 980 $m^2\ g^{-1}$, in contrast with homochiral **CC4**-*R*, where a complex, stepped isotherm is observed as a result of the window-to-arene packing in that system.[71] Likewise, the quasi-racemic (**CC3**-*R*, **CC4**-*S*) particles prepared by mixing at 20 °C showed a standard type I isotherm with SA_{BET} = 936 $m^2\ g^{-1}$ (Figures S10 and S11). These surface areas, while lower than some extended networks,[20] are among the highest reported for porous molecular solids.[59−70]

Particle Size and Morphology Control Using Mixing Rate. The rate of addition of the two solutions during mixing was also found to affect both the particle morphology and the porosity in the materials. Most samples in this study were prepared using a relatively slow mixing rate of 0.5 mL min^{-1}. However, if the two solutions of opposite chirality were mixed rapidly, causing almost an immediate precipitation, then spherical particles were produced. Both the micropore volume and the surface area in these rapidly precipitated particles were increased with respect to materials produced by slower mixing. Rapid mixing of **CC3**-*R* and **CC3**-*S* at 20 °C gave reproducible apparent BET surface areas of more than 900 $m^2\ g^{-1}$ (Figures 6d and S12). This represents a 50% increase in surface area in comparison with the homochiral form of **CC3** (624 $m^2\ g^{-1}$),[59] and this cannot easily be rationalized by particle size alone. Moreover, DLS and SEM measurements showed that the rate of mixing did not affect the size of the particles significantly (Figure S13). However, SEM investigations did show a marked morphology change for

CC3-(*R*,*S*) samples produced by more rapid mixing (Figure 7a). Slow mixing gave rise to octahedral crystals. As the mixing rate is increased, this geometry becomes increasingly more spherical. Octahedron-shaped particles represent the ideal crystal morphology that is predicted from the crystal structure model (Figure 7b; details in Supporting Information). We suggest, therefore, that the substantial increase in microporosity for rapidly mixed samples stems from increased disorder within the crystals, resulting from rapidly induced precipitation. There are some precedents for disorder enhancing microporosity. For example, a recent study has revealed that small defects in the crystal structure, unobserved by X-ray diffraction, can play a key role in determining the porosity and surface area in MOFs.[81,82] Based on these observations, the influence of molecular disorder was explored in greater detail, as described in the next section.

Table 1. DFT-D3 Calculated Binding Energies for Isolated Cage Pairs for the Systems Discussed Here[a]

cage pair	Packing mode	binding energy (kJ mol^{-1})
CC3-*R*/**CC3**-*R*	**window-to-window**	**−150**
	window-to-arene	−55
	arene-to-arene	−67
CC3-*R*/**CC3**-*S*	**window-to-window**	**−169**
	window-to-arene	−68
	arene-to-arene	−82
CC4-*R*/**CC4**-*R*	window-to-window	−77
	window-to-arene	**−110**
	arene-to-arene	−90
CC4-*R*/**CC4**-*S*	**window-to-window**	**−167**
	window-to-arene	−110
	arene-to-arene	−90
CC3-*R*/**CC4**-*S*	**window-to-window**	**−162**
CC3-*R*/**CC4**-*R*	window-to-window	−127

[a] The most favorable packing mode for each cage pair is highlighted in bold.

It is also possible to combine the effects of mixing rate and mixing temperature. To demonstrate this, a **CC3**-(*R*,*S*) sample was produced by rapidly mixing (>20 mL min^{-1}) the **CC3**-*R* and **CC3**-*S* enantiomers at −80 °C. This produced irregular particles with mixed morphology and an average size of just 30 nm, as measured by electron microscopy (Figure S14). Gas sorption measurements show evidence for both microporosity and mesoporosity (Figure 7c); again, we attribute the latter to interparticulate voids. The BET surface area, 819 m^2 g^{-1}, was higher than that of the bulk crystalline phase of homochiral **CC3**-*R*. The contribution of interparticulate space is now significant, as evidenced by the total N_2 uptake of 22.8 mmol g^{-1} for these racemic nanoparticles compared with 8.2 mmol g^{-1} for macroscopic homochiral **CC3**-*R* crystals.[59]

Rationalization of Porosity: Crystalline or Amorphous? The racemic crystals and quasi-racemic cocrystals reported here all pack in an analogous window-to-window fashion, resulting in a 3-D diamondoid pore structure that runs throughout the structure (Figure 1). While this makes full use of the internal porosity in each cage module, the external molecular surface of the cage molecules is not exploited. We have already shown that fully amorphous cage materials, produced by purposeful molecular scrambling reactions,[64] can exhibit more porosity than their crystalline analogues because they exploit both "intrinsic" porosity (in the cages) and "extrinsic" porosity (between the cages).[67] Microporosity has also been observed in other fully amorphous organic molecular solids.[19,83] One hypothesis,

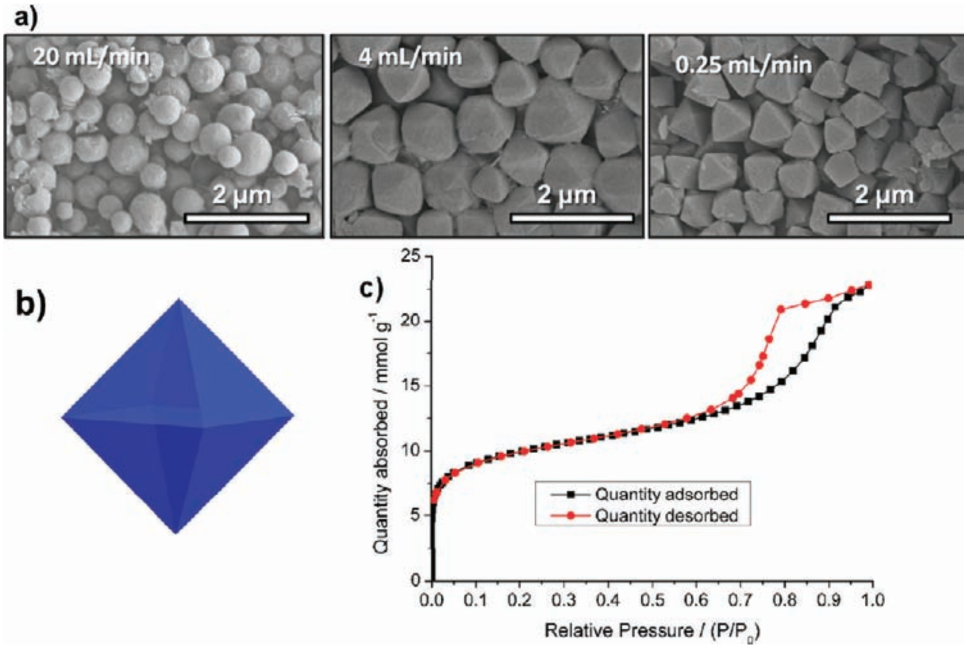

Figure 7. (a) Scanning electron micrographs for racemic **CC3**-(*R*,*S*) crystals formed by mixing dichloromethane solutions of the homochiral modules at different rates of addition. (b) Morphology prediction for crystal growth based on a Wulff plot generated from the **CC3**-(*R*,*S*) crystal structure. (c) N_2 sorption isotherm (77 K) for **CC3**-(*R*,*S*) particles produced by mixing solutions rapidly (>20 mL min^{-1}) at −80 °C; SA_{BET} = 819 m^2 g^{-1}.

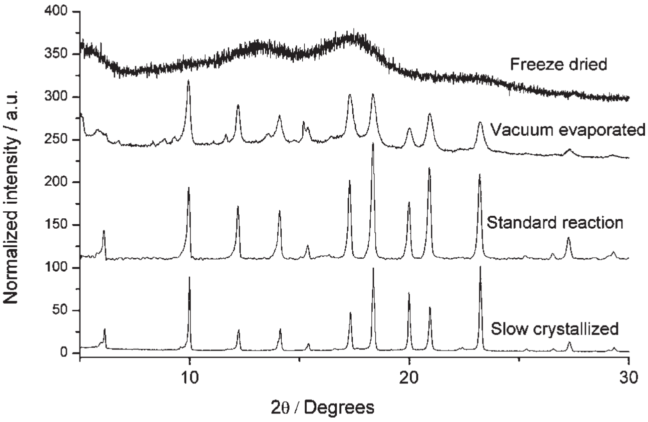

Figure 8. Powder X-ray diffraction patterns of **CC3**-*R* produced by freeze-drying, vacuum evaporation, standard reaction, and slow crystallization. It can be noted that the freeze-dried sample is amorphous, and that a broadening of peaks can be observed in the other samples increasing in accordance with the expected decrease in crystallinity.

therefore, is that the increased surface area in these racemic and quasi-racemic particles results from a reduction in crystallinity, in keeping with some of the morphologies observed by SEM, particularly for rapidly mixed samples (Figure 7a).

To investigate the influence of the rate of precipitation from solution, a series of control experiments was performed with homochiral **CC3**-*R*. The objective was to investigate the connection between precipitation rate and crystallinity, and whether this in turn influences the resultant porosity and surface area, as suggested by the racemic and quasi-racemic particles described above. To do this, **CC3**-*R* was isolated from solution by a variety of routes. First, six samples of **CC3**-*R* were synthesized in parallel and allowed to crystallize slowly from the reaction mixture in order to produce large crystals ($d > 500\ \mu$m)—that is, to maximize the degree of crystallinity. A further six samples of **CC3**-*R* were dissolved in DCM, frozen rapidly in liquid nitrogen, and then freeze-dried. The aim was to induce rapid precipitation from solution and to render the **CC3**-*R* material, as far as possible, in an amorphous state. Six repeats in each case were carried out to establish the reproducibility of the procedures. These 12 samples were also compared to a sample produced directly by our standard synthesis (as described in the Methods section), and a further sample that was rapidly precipitated from solution by fast vacuum evaporation of the solvent, rather than by freeze-drying.

The six slow-crystallized samples all appeared to be crystalline on the basis of PXRD measurements, as did both the sample produced via our "standard" reaction and the fast vacuum-evaporated sample. However, the vacuum-evaporated sample showed a marked broadening of PXRD peak widths (Figure 8). Moreover, upon close inspection it was clear that the slow-crystallized samples gave rise to significantly narrower PXRD peaks than the material produced directly by our standard synthesis. By contrast, each of the six freeze-dried samples appeared to be close to amorphous on the basis of PXRD. SEM imaging of the samples supported these PXRD observations. Regular octahedral crystals were observed for the slow-crystallized samples and the standard reaction sample, while irregular morphologies were seen for the fast vacuum-evaporated and freeze-dried samples (Figure S15).

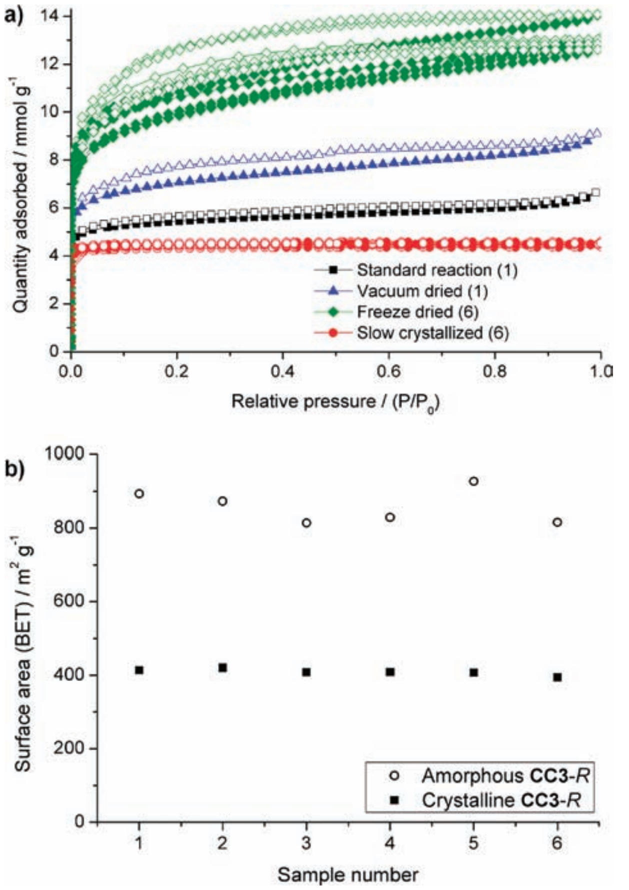

Figure 9. (a) N_2 sorption isotherms (77 K) for **CC3**-*R* produced by freeze-drying (green diamonds), vacuum evaporation (blue triangles), standard reaction (black squares), and slow crystallization (red circles). Closed symbols show the adsorption isotherms and open symbols show the desorption isotherms. (b) Reproducibility in surface area shown for the crystalline (black squares) and amorphous (open circles) **CC3**-*R* produced by slow crystallization and freeze-drying, respectively.

There is a direct correlation between the rate of precipitation and both the gas uptakes and the calculated apparent BET surface areas in this series of samples (Figure 9). The slow-crystallized samples show a classic type I isotherm with no hysteresis,[80] consistent with an ordered crystalline structure with a narrow micropore distribution. This was extremely reproducible: Figure 9 shows the overlay of the nitrogen adsorption/desorption isotherms for all six repeat crystallizations, and an apparent $SA_{BET} = 409\ m^2\ g^{-1}$ was derived with a standard deviation of just $8\ m^2\ g^{-1}$ (see Figure 9b).

The freeze-dried samples showed a much higher nitrogen uptake of $13.3 \pm 0.6\ mmol\ g^{-1}$ at $P/P_0 = 1$, as compared with an uptake of $4.50 \pm 0.07\ mmol\ g^{-1}$ for the slow-crystallized material. A type I isotherm was again observed; however, in this case both the sorption and the desorption curves are sloped at higher relative pressures, and some hysteresis is observed. This is consistent with the introduction of a degree of mesoporosity and a broader range of pore sizes. The apparent BET surface area for the amorphous samples was, on average, more than twice that calculated for the slow-crystallized samples ($859\ m^2\ g^{-1}$; standard deviation = $63\ m^2\ g^{-1}$). The increased sample-to-sample variation in the isotherms and in the calculated BET surface areas for these six samples (Figure 9) is perhaps to be expected from the nature of

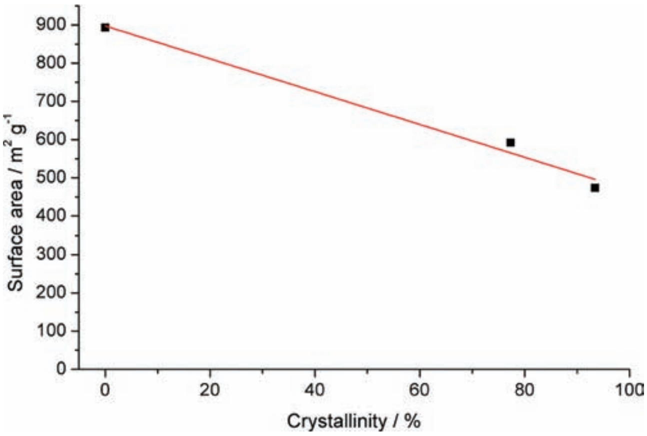

Figure 10. Comparison between surface area and percentage crystallinity for highly crystalline, intermediately crystalline, and amorphous samples of **CC3**-*R*.

the rapid freezing—freeze-drying process. These results are consistent with the hypothesis that rapid precipitation induces lower crystallinity and, hence, a higher accessible surface area in the solids. We rationalize this as stemming from increased extrinsic porosity that becomes accessible in the less ordered materials.

We next attempted to make a quantitative comparison between the apparent BET surface area and the level of crystallinity in **CC3**-*R* (Figure 10). To do this, the percentage crystallinity was determined by whole-profile pattern fitting of the powder diffraction profiles to estimate the relative contributions from the amorphous and crystalline phases (see details in Supporting Information). Pawley refinement[84] was used to extract a model of the diffraction intensities in the PXRD pattern for the fully amorphous, freeze-dried samples. This was then used in a multiphase refinement of the powder patterns for highly crystalline and intermediately crystalline samples (Figure S16). With the intensities of individual reflections fixed, the refined scale factors of the crystalline and amorphous phases were used to calculate the relative abundance of the crystalline phase. For the samples analyzed, we observed an approximately linear relationship between the level of crystallinity in **CC3**-*R* and the apparent BET surface area for the sample (Figure 10). On the basis of this analysis, even a slow-crystallized sample was calculated to be imperfectly crystalline (93%). Nonetheless, the porosity in these slow-crystallized **CC3**-*R* materials can be considered to arise predominantly from the ordered, crystalline structure in the materials (Figure 1). By contrast, the as-synthesized, "standard" **CC3**-*R* reaction leads to a material with intermediate crystallinity (77%) and an apparent BET surface area (592 m^2 g^{-1}) that is significantly higher than the slow-crystallized materials (409 ± 8 m^2 g^{-1}). We suggest that this difference stems from increased disorder in the as-prepared sample; that is, disorder enhances the level of porosity in these solids, while broadening the micro-/mesopore size distribution (see also comparison of calculated pore size distributions, Figure S17).

On the basis of these data, it is reasonable to suggest that the enhanced surface areas observed for the rapidly precipitated racemic and quasi-racemic particles arise from a reduction in crystalline order. We propose that rapidly induced crystallization causes a reduction in long-range order in comparison to more slowly crystallized samples. This could lead to an increase in voids and defects, and to particles comprising misaligned nanocrystalline phases, hence creating additional extrinsic microporosity between the cages. The higher apparent BET surface areas in the **CC4**-(*R*,*S*) and (**CC3**-*R*, **CC4**-*S*) particles prepared at 20 °C (980 and 936 m^2 g^{-1}, respectively) compared to the equivalent **CC3**-(*R*,*S*) sample (696 m^2 g^{-1}) might therefore be explained by the more pronounced solubility suppression in those systems upon mixing (see discussion above and Figure S7). We propose that precipitation is more rapid upon mixing the constituent modules for **CC4**-(*R*,*S*) and for (**CC3**-*R*, **CC4**-*S*), and hence greater disorder and more microporosity is introduced.

DISCUSSION

We demonstrate here a solution mixing process for the preparation of highly microporous particles with apparent BET surface areas of up to ~950 m^2 g^{-1}. As evidenced by the video included online with Figure 3, the procedure is very simple in comparison with other methods for the production of microporous particles. Moreover, particle sizes are highly uniform and can be controlled in the size range from 30 nm to 1 μm by varying the mixing temperature, the mixing speed, or both. This may have practical implications, for example, in the preparation of materials for adsorption, for chromatographic separations, or for heterogeneous catalysis. The process also leads to organic dispersions that are stable for at least months in the absence of any surfactants (Figure 3), suggesting additional applications such as the formation of microporous coatings or the preparation of composite materials where microporous organic nanoparticles are deposited within a secondary host.

The porosity in these materials is influenced by the particle size, especially in the case of small particles ($d < 100$ nm) where interparticulate voids and external particle surfaces begin to play a significant role. Of perhaps even greater significance, however, is the degree of crystallinity in the materials. The experiments with **CC3**-*R* (Figures 9 and 10) show clearly that fully amorphized samples are much more porous than their crystalline analogues: Indeed, fully amorphous **CC3**-*R* adsorbs almost three times as much N$_2$ as crystalline **CC3**-*R* and has over twice the apparent BET surface area. Materials with intermediate degrees of crystallinity have intermediate levels of porosity. For example, on the basis of these new data, we estimate that **CC3**-*R* (SA_{BET} = 624 m^2 g^{-1}) as prepared in our first study[59] was around 75—80% crystalline, while more purely crystalline **CC3**-*R*, prepared by slow crystallization, has a somewhat lower and highly reproducible surface area of 409 ± 8 m^2 g^{-1}. As illustrated in Figure 8 (and also Figure S18), the difference between the PXRD patterns for samples with differing degrees of crystallinity and microporosity may be relatively subtle, as mostly expressed by a broadening in the Bragg peaks. This observation has direct relevance to any studies involving crystalline porous organic molecular solids, and perhaps especially for cage-like materials comprising prefabricated pore volume[59,62,66] where intrinsic porosity may be covalently protected with respect to amorphization.

We also speculate that these observations regarding the influence of molecular disorder on microporosity might have broader relevance in terms of porous crystalline frameworks. There is often a perception that amorphous "impurities" in materials such as MOFs and COFs will be denser than the crystalline framework, and hence serve to lower porosity and accessible surface area. There is no fundamental reason, however, for this to be the case. Indeed, the material with the highest reported BET surface area, at the time of writing, is a wholly amorphous porous polymer framework[85−87] ($SA_{BET} = 6461$ m^2 g^{-1}).[87] Likewise, amorphous covalent triazine frameworks (CTFs) prepared from 1,4-dicyanobenzene were found to be more porous than their semicrystalline analogues.[9,88,89] A number of COFs give rise to PXRD patterns with rather broad peaks and sample morphologies that, in some cases, do not immediately suggest long-range order or crystalline phases. Indeed, COF-1,[8,90] COF-5,[8,12,13] COF-300,[11] and the triazine framework, CTF-1,[9] for example, all give rise to PXRD peaks of breadth roughly comparable to those observed here for **CC3**-*R* with intermediate crystallinity.[91] Moreover, the N_2 gas sorption isotherm and pore size distribution data for COF-1[8] are more similar to those of **CC3**-*R* with intermediate crystallinity, rather than the most crystalline **CC3**-*R* materials (Figure 9 and Figure S17), although it should be noted that the two materials do not have identical pore sizes. Clearly, all of these extended COF materials, like the molecular cages studied here, exhibit long-range order based on PXRD and other analyses. It is conceivable, however, that disorder also contributes to the microporosity in COFs while being relatively invisible to techniques such as PXRD, just as observed for **CC3**-*R*. For example, COF-1, COF-5 and CTF-1 all have 1,3,5-connected topologies, and one could envisage chemically plausible amorphous models that rationalize microporosity, much as we have presented for 1,3,5-connected amorphous conjugated microporous polymers (CMPs).[15,16] Likewise, it might also be possible to conceive amorphous models that rationalize porosity in COF-300, as we suggested for the tetrahedral polymer framework, PAF-1.[18,85] On the basis of available characterization data, it is difficult to quantify the contribution (if any) of disorder to porosity in these crystalline COFs. In light of our new findings, however, we would recommend that researchers consider this potential contribution to porosity when analyzing crystalline frameworks and porous molecular crystals.

CONCLUSIONS

We introduce here a new, modular approach to the bottom-up fabrication of microporous particles that allows fine control over particle size. The method is extremely simple, and involves no more than mixing together solutions of organic cage modules with opposite chirality. The cage modules themselves are readily synthesized on multigram scales in a one-pot synthesis in good yields (80−90%).[92] Both the size and shape of the particles can be controlled, as can the level of microporosity and mesoporosity. Apparent BET surface areas approaching 1000 m^2 g^{-1} can be obtained. Dispersions and nanodispersions of these porous particles are stable in organic solvents for at least several months, and no additional workup or purification is required because no surfactants or templates are used. In principle, this methodology could be extended to larger cage modules—for example, to prepare porous nanoparticles for drug delivery applications. Likewise, the method need not be limited to chiral recognition, but could be extended to any cage combination where the solubility of the cocrystal is significantly lower than that of the individual modules. In this regard, there is much scope for the synthetic introduction of chemical recognition motifs in cages—for example, to enable intermolecular interactions such as hydrogen bonding, halogen bonding,[67] salt formation, and $\pi-\pi$ stacking.

In the course of the study, we have also demonstrated the importance of molecular disorder in these systems. Indeed, if the end goal is simply to enhance surface area, total amorphization can greatly enhance porosity, although this also leads to a broader pore size distribution. We believe that this latter observation might have much wider relevance—for example, when evaluating structure−property relationships in predominantly crystalline extended frameworks such as MOFs and COFs.

ASSOCIATED CONTENT

Ⓢ **Supporting Information.** NMR spectra and solubility studies, electron microscopy, crystallographic and computer simulation details, gas sorption isotherms and PXRD patterns. This material is available free of charge via the Internet at http://pubs.acs.org.

Ⓦ **Web Enhanced Feature.** A video file showing an example of **CC3**-*R*/**CC3**-*S* solution mixing experiment is available online.

AUTHOR INFORMATION

Corresponding Author

aicooper@liv.ac.uk

ACKNOWLEDGMENT

We thank the Engineering and Research Council for financial support under grant EP/H000925/1. A.I.C. is a Royal Society Wolfson Research Merit Award holder. We thank Mr. Rob Clowes for gas sorption analysis and Dr. Sean Higgins for assistance with robotic liquid handlers. We thank Diamond Light Source for access to beamline I11 and Prof. Chui Tang, Dr. Julia Parker, and Dr. Alistair Lennie for their assistance during the experiment.

REFERENCES

(1) *Handbook of Porous Solids*; Schüth, F., Sing, K. S. W., Weitkamp, J., Eds.; Wiley VCH: Heidelberg, 2002.

(2) Wright, P. A. *Microporous Framework Solids*; Royal Society of Chemistry: Cambridge, UK, 2008.

(3) Yaghi, O. M.; Li, H. L.; Davis, C.; Richardson, D.; Groy, T. L. *Acc. Chem. Res.* **1998**, *31*, 474.

(4) Cheetham, A. K.; Férey, G.; Loiseau, T. *Angew. Chem., Int. Ed.* **1999**, *38*, 3268.

(5) Kitagawa, S.; Kitaura, R.; Noro, S. *Angew. Chem., Int. Ed.* **2004**, *43*, 2334.

(6) Bradshaw, D.; Claridge, J. B.; Cussen, E. J.; Prior, T. J.; Rosseinsky, M. J. *Acc. Chem. Res.* **2005**, *38*, 273.

(7) Li, J. R.; Kuppler, R. J.; Zhou, H. C. *Chem. Soc. Rev.* **2009**, *38*, 1477.

(8) Côté, A. P.; Benin, A. I.; Ockwig, N. W.; O'Keeffe, M.; Matzger, A. J.; Yaghi, O. M. *Science* **2005**, *310*, 1166.

(9) Kuhn, P.; Antonietti, M.; Thomas, A. *Angew. Chem., Int. Ed.* **2008**, *47*, 3450.

(10) El-Kaderi, H. M.; Hunt, J. R.; Mendoza-Cortes, J. L.; Côté, A. P.; Taylor, R. E.; O'Keeffe, M.; Yaghi, O. M. *Science* **2007**, *316*, 268.

(11) Uribe-Romo, F. J.; Hunt, J. R.; Furukawa, H.; Klock, C.; O'Keeffe, M.; Yaghi, O. M. *J. Am. Chem. Soc.* **2009**, *131*, 4570.

(12) Furukawa, H.; Yaghi, O. M. *J. Am. Chem. Soc.* **2009**, *131*, 8875.

(13) Ritchie, L. K.; Trewin, A.; Reguera-Galan, A.; Hasell, T.; Cooper, A. I. *Microporous Mesoporous Mater.* **2010**, *132*, 132.

(14) Colson, J. W.; Woll, A. R.; Mukherjee, A.; Levendorf, M. P.; Spitler, E. L.; Shields, V. B.; Spencer, M. G.; Park, J.; Dichtel, W. R. *Science* **2011**, *332*, 228.

(15) Jiang, J. X.; Su, F.; Trewin, A.; Wood, C. D.; Campbell, N. L.; Niu, H.; Dickinson, C.; Ganin, A. Y.; Rosseinsky, M. J.; Khimyak, Y. Z.; Cooper, A. I. *Angew. Chem., Int. Ed.* **2007**, *46*, 8574.

(16) Jiang, J. X.; Trewin, A.; Su, F. B.; Wood, C. D.; Niu, H. J.; Jones, J. T. A.; Khimyak, Y. Z.; Cooper, A. I. *Macromolecules* **2009**, *42*, 2658.

(17) Jiang, J.-X.; Cooper, A. I. *Top. Curr. Chem.* **2010**, *293*, 1.

(18) Trewin, A.; Cooper, A. I. *Angew. Chem., Int. Ed.* **2010**, *49*, 1533.

(19) McKeown, N. B.; Budd, P. M. *Macromolecules* **2010**, *43*, 5163.

(20) Holst, J. R.; Cooper, A. I. *Adv. Mater.* **2010**, *22*, 5212.

(21) McKeown, N. B.; Budd, P. M. *Chem. Soc. Rev.* **2006**, *35*, 675.

(22) Merkel, T. C.; Freeman, B. D.; Spontak, R. J.; He, Z.; Pinnau, I.; Meakin, P.; Hill, A. J. *Science* **2002**, *296*, 519.

(23) Sun, J. M.; Bao, X. H. *Chem.—Eur. J.* **2008**, *14*, 7478.

(24) Guihen, E.; Glennon, J. D. *Anal. Lett.* **2003**, *36*, 3309.

(25) Huxford, R. C.; Della Rocca, J.; Lin, W. B. *Curr. Opin. Chem. Biol.* **2010**, *14*, 262.

(26) Rhodes, K. H.; Davis, S. A.; Caruso, F.; Zhang, B. J.; Mann, S. *Chem. Mater.* **2000**, *12*, 2832.

(27) Chen, Y.; Fitz Gerald, J. D.; Chadderton, L. T.; Chaffron, L. *Appl. Phys. Lett.* **1999**, *74*, 2782.

(28) Jiang, H. L.; Liu, B.; Akita, T.; Haruta, M.; Sakurai, H.; Xu, Q. *J. Am. Chem. Soc.* **2009**, *131*, 11302.

(29) Papadimitrakopoulos, F.; Wisniecki, P.; Bhagwagar, D. E. *Chem. Mater.* **1997**, *9*, 2928.

(30) Cravillon, J.; Nayuk, R.; Springer, S.; Feldhoff, A.; Huber, K.; Wiebcke, M. *Chem. Mater.* **2011**, *23*, 2130.

(31) Hermes, S.; Witte, T.; Hikov, T.; Zacher, D.; Bahnmuller, S.; Langstein, G.; Huber, K.; Fischer, R. A. *J. Am. Chem. Soc.* **2007**, *129*, 5324.

(32) Tosheva, L.; Valtchev, V. P. *Chem. Mater.* **2005**, *17*, 2494.

(33) Chalati, T.; Horcajada, P.; Gref, R.; Couvreur, P.; Serre, C. *J. Mater. Chem.* **2011**, *21*, 2220.

(34) Garay, A. L.; Pichon, A.; James, S. L. *Chem. Soc. Rev.* **2007**, *36*, 846.

(35) Falcaro, P.; et al. *Nat. Commun.* **2011**, *2*, 237.

(36) Schwab, M. G.; Senkovska, I.; Rose, M.; Koch, M.; Pahnke, J.; Jonschker, G.; Kaskel, S. *Adv. Eng. Mater.* **2008**, *10*, 1151.

(37) O'Neill, L. D.; Zhang, H. F.; Bradshaw, D. *J. Mater. Chem.* **2010**, *20*, 5720.

(38) Macintyre, F. S.; Sherrington, D. C.; Tetley, L. *Macromolecules* **2006**, *39*, 5381.

(39) Larsen, S. C. *J. Phys. Chem. C* **2007**, *111*, 18464.

(40) Holmberg, B. A.; Wang, H. T.; Norbeck, J. M.; Yan, Y. S. *Microporous Mesoporous Mater.* **2003**, *59*, 13.

(41) Mintova, S.; Olson, N. H.; Valtchev, V.; Bein, T. *Science* **1999**, *283*, 958.

(42) Schoeman, B. J.; Sterte, J.; Otterstedt, J. E. *Zeolites* **1994**, *14*, 110.

(43) Zhu, G. S.; Qiu, S. L.; Yu, J. H.; Sakamoto, Y.; Xiao, F. S.; Xu, R. R.; Terasaki, O. *Chem. Mater.* **1998**, *10*, 1483.

(44) Huang, Y.; Wang, K.; Dong, D. H.; Li, D.; Hill, M. R.; Hill, A. J.; Wang, H. T. *Microporous Mesoporous Mater.* **2010**, *127*, 167.

(45) Zhan, B. Z.; White, M. A.; Lumsden, M.; Mueller-Neuhaus, J.; Robertson, K. N.; Cameron, T. S.; Gharghouri, M. *Chem. Mater.* **2002**, *14*, 3636.

(46) Madsen, C.; Jacobsen, C. J. H. *Chem. Commun.* **1999**, 673.

(47) Wang, H. T.; Holmberg, B. A.; Yan, Y. S. *J. Am. Chem. Soc.* **2003**, *125*, 9928.

(48) Li, Y. S.; Bux, H.; Feldhoff, A.; Li, G. L.; Yang, W. S.; Caro, J. *Adv. Mater.* **2010**, *22*, 3322.

(49) Diring, S.; Furukawa, S.; Takashima, Y.; Tsuruoka, T.; Kitagawa, S. *Chem. Mater.* **2010**, *22*, 4531.

(50) Spokoyny, A. M.; Kim, D.; Sumrein, A.; Mirkin, C. A. *Chem. Soc. Rev.* **2009**, *38*, 1218.

(51) Ma, M.; Zacher, D.; Zhang, X. N.; Fischer, R. A.; Metzler-Nolte, N. *Cryst. Growth Des.* **2011**, *11*, 185.

(52) Horcajada, P.; et al. *Nat. Mater.* **2010**, *9*, 172.

(53) McKinlay, A. C.; Morris, R. E.; Horcajada, P.; Ferey, G.; Gref, R.; Couvreur, P.; Serre, C. *Angew. Chem., Int. Ed.* **2010**, *49*, 6260.

(54) Lin, W. B.; Rieter, W. J.; Taylor, K. M. L. *Angew. Chem., Int. Ed.* **2009**, *48*, 650.

(55) Rieter, W. J.; Taylor, K. M. L.; An, H. Y.; Lin, W. L.; Lin, W. B. *J. Am. Chem. Soc.* **2006**, *128*, 9024.

(56) Barrer, R. M.; Shanson, V. H. *J. Chem. Soc., Chem. Commun.* **1976**, 333.

(57) Atwood, J. L.; Barbour, L. J.; Jerga, A. *Science* **2002**, *296*, 2367.

(58) Barbour, L. J. *Chem. Commun.* **2006**, 1163.

(59) Tozawa, T.; et al. *Nat. Mater.* **2009**, *8*, 973.

(60) McKeown, N. B. *J. Mater. Chem.* **2010**, *20*, 10588.

(61) Holst, J. R.; Trewin, A.; Cooper, A. I. *Nat. Chem.* **2010**, *2*, 915.

(62) Mastalerz, M.; Schneider, M. W.; Oppel, I. M.; Presly, O. *Angew. Chem., Int. Ed.* **2010**, *50*, 1046.

(63) Cooper, A. I. *Angew. Chem., Int. Ed.* **2011**, *50*, 996.

(64) Jiang, S.; Jones, J. T. A.; Hasell, T.; Blythe, C. E.; Adams, D. J.; Trewin, A.; Cooper, A. I. *Nature Commun.* **2011**, *2*, 207.

(65) Jones, J. T. A.; Holden, D.; Mitra, T.; Hasell, T.; Adams, D. J.; Jelfs, K. E.; Trewin, A.; Willock, D. J.; Day, G. M.; Bacsa, J.; Steiner, A.; Cooper, A. I. *Angew. Chem., Int. Ed.* **2011**, *50*, 749.

(66) Jones, J. T. A.; Hasell, T.; Wu, X. F.; Bacsa, J.; Jelfs, K. E.; Schmidtmann, M.; Chong, S. Y.; Adams, D. J.; Trewin, A.; Schiffman, F.; Cora, F.; Slater, B.; Steiner, A.; Day, G. M.; Cooper, A. I. *Nature* **2011**, *474*, 367.

(67) Bojdys, M. J.; Briggs, M. E.; Jones, J. T. A.; Adams, D. J.; Chong, S. Y.; Schmidtmann, M.; Cooper, A. I. *J. Am. Chem. Soc.* **2011**, *133*, 16566.

(68) Hasell, T.; Schmidtmann, M.; Cooper, A. I. *J. Am. Chem. Soc.* **2011**, *133*, 14920.

(69) Bezzu, C. G.; Helliwell, M.; Warren, J. E.; Allan, D. R.; McKeown, N. B. *Science* **2010**, *327*, 1627.

(70) Tranchemontagne, D. J. L.; Ni, Z.; O'Keeffe, M.; Yaghi, O. M. *Angew. Chem., Int. Ed.* **2008**, *47*, 5136.

(71) Mitra, T.; Wu, X.; Clowes, R.; Jones, J. T. A.; Jelfs, K. E.; Adams, D. J.; Trewin, A.; Bacsa, J.; Steiner, A.; Cooper, A. I. *Chem.—Eur. J.* **2011**, *17*, 10235.

(72) Wheeler, K. A.; Grove, R. C.; Davis, R. E.; Kassel, W. S. *Angew. Chem., Int. Ed.* **2008**, *47*, 78.

(73) Coelho, A. A. *TOPAS-Academic*, version 4.1, 2007; http://www.topas-academic.net.

(74) Price, S. L. *Acc. Chem. Res.* **2009**, *42*, 117.

(75) Day, G. M.; et al. *Acta Crystallogr. Sect. B, Struct. Sci.* **2009**, *65*, 107.

(76) VandeVondele, J.; Krack, M.; Mohamed, F.; Parrinello, M.; Chassaing, T.; Hutter, J. *Comput. Phys. Commun.* **2005**, *167*, 103.

(77) Becke, A. D. *Phys. Rev. A* **1988**, *38*, 3098.

(78) VandeVondele, J.; Hutter, J. *J. Chem. Phys.* **2007**, *127*, 114105.

(79) Hasell, T.; Wu, X. F.; Jones, J. T. A.; Bacsa, J.; Steiner, A.; Mitra, T.; Trewin, A.; Adams, D. J.; Cooper, A. I. *Nat. Chem.* **2010**, *2*, 750.

(80) Rouquerol, F.; Rouquerol, J.; Sing, K. *Adsorption by Powders and Porous Solids*; Academic Press: London, 1999.

(81) Hibbe, F.; Chmelik, C.; Heinke, L.; Pramanik, S.; Li, J.; Ruthven, D. M.; Tzoulaki, D.; Kärger, J. R. *J. Am. Chem. Soc.* **2011**, *133*, 2804.

(82) Sholl, D. S. *Nat. Chem.* **2011**, *3*, 429.

(83) Tian, J.; Thallapally, P. K.; Dalgarno, S. J.; McGrail, P. B.; Atwood, J. L. *Angew. Chem., Int. Ed.* **2009**, *48*, 5492.

(84) Pawley, G. S. *J. Appl. Crystallogr.* **1981**, *14*, 357.

(85) Ben, T.; Ren, H.; Ma, S. Q.; Cao, D. P.; Lan, J. H.; Jing, X. F.; Wang, W. C.; Xu, J.; Deng, F.; Simmons, J. M.; Qiu, S. L.; Zhu, G. S. *Angew. Chem., Int. Ed.* **2009**, *48*, 9457.

(86) Holst, J. R.; Stöckel, E.; Adams, D. J.; Cooper, A. I. *Macromolecules* **2010**, *43*, 8531.

(87) Yuan, D.; Lu, W.; Zhao, D.; Zhou, H.-C. *Adv. Mater.* **2011**, *23*, 3723–3725.

(88) Kuhn, P.; Forget, A.; Su, D. S.; Thomas, A.; Antonietti, M. *J. Am. Chem. Soc.* **2008**, *130*, 13333.

(89) Zhang, W.; Li, C.; Yuan, Y. P.; Qiu, L. G.; Xie, A. J.; Shen, Y. H.; Zhu, J. F. *J. Mater. Chem.* **2010**, *20*, 6413.

(90) Musa, M. A. A.; Yin, C. Y.; Savory, R. M. *Mater. Chem. Phys.* **2010**, *123*, 5.

(91) In the case of crystalline CTF-1,[9] the PXRD peaks are substantially broader than observed for any of the crystalline **CC3**-*R* samples here.

(92) Lydon, D. P.; Campbell, N. L.; Adams, D. J.; Cooper, A. I. *Synth. Commun.* **2011**, *41*, 2146.